The effects of dopant impurities on Cu_2ZnSnS_4 system Raman properties

Prashant K. Sarswat · Michael L. Free

Abstract Impurities in Cu_2ZnSnS_4 (CZTS) can alter the electronic and optical properties, which may reduce photovoltaic device efficiency. Phonon dispersion susceptibility can be used to investigate the effects of foreign dopants on pairing between atoms within lattice. In order to investigate the effect of free holes on the optical phonons and asymmetry in the Raman peaks due to impurities, Sb-, Fe-, and Ag-doped CZTS thin films were prepared and systematically studied. Doping with impurities causes a shift in Raman peak frequency as well as linewidth. An investigation has been made based on the reduced mass of the vibrating CZTS lattice that changes due to dopant addition. For polycrystalline Sb-doped CZTS, the predicted wavenumber shift for Raman 'A' mode follows a similar trend as evidenced in experiments and can be explained by the square-root relationship between frequency and the vibrating mass. Raman lineshape for Sb-doped CZTS thin films and nanocrystals becomes wider, asymmetric, and moves toward lower vibrational frequency when laser power density increases. Atomic force microscopy was also performed to examine surface properties.

P. K. Sarswat (✉)
Department of Metallurgical Engineering, University of Utah, 135 S, 1460 E, Room 412, Salt Lake City, UT 84112, USA
e-mail: saraswatp@gmail.com

M. L. Free
Department of Metallurgical Engineering, University of Utah, 135 S, 1460 E, Room 417, Salt Lake City, UT 84112, USA
e-mail: michael.free@utah.edu

Introduction

Relatively new, thin-film absorber materials such as Cu–Zn–Sn–S (CZTS) that are environmentally friendly and earth abundant offer great potential for use in photovoltaic, electronic, and sensor applications. $Cu_2ZnSnS_xSe_{4-x}$ (CZTSSe), a quaternary chalcogenide system, has gained significant attention as a p-type photovoltaic absorber layer due to its attractive properties such as high absorption coefficient, optimum band gap, and use of low cost elements. High power conversion efficiency ~ 12 % has been reported for CZTS solar cells that have been fabricated from solution-based techniques on a laboratory scale [1]. Efficiency can be improved by optimizing processing parameters that correlate with microstructure and crystal quality of absorber layers or stacks. One of the ways to improve photovoltaic film quality is to produce electrically benign grain boundaries by adding foreign impurities. The addition of foreign impurities or doping causes changes in various fundamental physical properties such as defect stability, charge carrier transport, photoelectrochemical behavior, phase stability, and electronic structure [2–4]. For CZTS and structurally similar compounds, Raman spectroscopy is one of the most widely used measurement techniques for phase and defect analysis. Using this technique, quantum interference and interband electronic Raman scattering processes can be investigated, which is still lacking for CZTS. It is important to note that the effects of doping on CZTS properties such as surface topography, grain boundary conductivity, band gap, absorption coefficient, and charge carrier concentration are not well understood. Improved understanding of the related phenomena such as phonon dispersion and background-resonant scattering interference will enable more effective use of these materials in devices needed in the future.

Background

Phonon dispersion in most semiconductors is found to be sensitive to the coupling between the atoms within the lattice [5, 6]. Hence, a variation in phonon dispersion as observed through shifts in Raman peaks can be used to investigate the effects of foreign impurities on atom coupling [5, 6]. Defect distributions and impurities in chalcogenide semiconductor absorber layer can alter the physical and electronic properties such as band gap, conductivity, photon absorption, trap level energy as well as external quantum efficiency, and open circuit potential of photovoltaic devices [7–9]. Such a conclusion was also validated by first principle calculations [10]. As semiconductor research activity continues to advance the limits of device dimensions, non-invasive tools such as Raman spectroscopy can be ideal to investigate the properties of doped semiconductors [11]. It is important to note that limited research has been done on interband electronic Raman scattering, although some research has focused on inter-valence band scattering in Cu–Zn–Sn–S systems [12]. Correspondingly, additional understanding regarding optical transitions and excited phonons is needed. This need can be achieved by conducting a detailed investigation of the effect of free holes on the optical phonons of doped CZTS as well as the asymmetry in the Raman line shape of the zone-centered optical phonon and local vibration modes.

There are several phenomena which can explain a change in line shape and/or asymmetry [5]. One aspect of defining asymmetry is 'phonon confinement'. Phonon confinement was observed for nanostructured CZTS material as well as polycrystalline CZTS film [5, 6]. In the case of phonon confinement in nanosize crystals, phonon momentum is uncertain, and there is a relaxation of momentum conservation [6]. Due to contributions of phonons to the Raman signal, the Raman peak may become more or less asymmetric depending on the phonon contribution. A widening peak can be associated with high energy or low energy [5]. Another aspect of the phonon confinement effect is the consideration of the effect of point and disorder defects. Lattice parameter evaluation from X-ray diffraction data suggests that increase in annealing time results in a small compressive strain [5]. Raman examination of CZTS film suggests that asymmetry could arise due to disordered distribution of Zn and Cu atoms in the sub-lattice. Such a distribution often results in a peak at ~ 332 cm^{-1}. However, it was observed that consideration of this peak and its Lorentzian contribution did not result in satisfactory spectral fitting. Results from the literature also suggest that asymmetry was also observed for other peaks [5]. Hence, the phonon confinement effect was deeply investigated by a few researchers for this type of system. Their results indicate that the Raman peak also downshifts and widens asymmetrically to

lower frequency with decreasing correlation length. Strain-induced effects often alter the frequency of Raman peaks. Hence, the cumulative effect of phonon confinement and strain are believed to be responsible for peak asymmetry. Both correlation length and grain size increase with the increase in annealing time [5]. It is important to mention here that sample prepared under conditions which result in smaller grain size is generally observed with more defects and shorter correlation length [5]. It was finally concluded that shapes of the peak's shift in peak frequency mainly depend on correlation length and strain effects [5].

A change in Raman line shapes sometime occurs when quantum interference occurs between two competing optical pathways: one connecting the energy ground state with an excited discrete state and the other linking the continuum of energy states with ground state [13, 14]. Such interference is known as Fano interference [15]. Theoretical investigations suggest that coherence induced by Fano interference or Fano coupling can enhance the power conversion efficiency, a photovoltaic cell compared to the same system without coherence [16]. It was also suggested that no additional external energy source is necessary to create such induced coherence [16]. The Fano effect has both detrimental and favorable outcomes, e.g., in the design of plasmonic solar cells [17]. Aluminum nanoparticles have capability to effectively lower the reflectance and increase the external quantum efficiency (EQE) of the bare multi crystalline-Si solar cells throughout the silicon absorption wavelength range [17]. Such an observation is different from other widely used Ag and Au nanoparticles, in which the EQE was found to decrease at short wavelengths. Use of Al nanoparticles causes a blue shift in Fano resonance to the wavelengths below the solar spectrum edge at 300 nm and therefore becomes harmless to the performance of the solar cells. Bulk GaAs shows a strong modification in the Fano profiles of the magneto-excitons due to resonant polaron coupling [18]. The origin of these modifications was identified as the resonant polaronic coupling between the charge carriers, which form the excitons, and longitudinal optical (LO) phonons, in conduction bands (CB) and valence bands (VB) [18].

In view of these research needs, a series of experiments were conducted to investigate the effect of free holes on the optical phonons of Cu–Zn–Sn–Sb–S as well as to evaluate asymmetry in the Raman line shape of the zone-centered optical phonons. It was reported that undoped CZTS, electronic transitions are possible from Cu-$3d(t_{2g})$/S-$3p^*$ to Sn-$5p$/Zn-$4s$/Cu-$4s$/S-$3p^*$ states (E1 transition), Cu-$3d(e_{2g})$/S-$3p^*$ to Sn-$5s$/S-$3p^*$, and Eo transition from Cu-$3d(t_{2g})$/S-$3p^*$ to Sn-$5s$/S-$3p^*$ states [19]. When exposed to incoming photons, doped CZTS possibly produces a continuum of inter-valence band electronic excitations, which can overlap the Raman-active phonon energy [20]. Such overlap between the electronic continuum and discrete states can

cause interference effects. Raman spectroscopy was utilized to investigate these effects. There is not much direct evidence of continuum of states. It is generally believed that such a system most likely possess the bound excitons [20]. However, broad deep level transient spectroscopy (DLTS) data for similar chalcogenide systems suggest a possibility of distribution of defect states as well as an appearance of smeared band edges [21].

The Raman peak becomes wider, asymmetric and shifts to lower frequency when the Raman spectra were collected with higher laser power density. All these observations were observed for Raman 'A' mode for Sb-doped samples as will be shown and discussed in this paper. S behavior can be attributed to the interference between discrete phonons and light-assisted electronic transitions. Such analysis of electron–phonon interactions under the framework of quantum interference can provide useful insights regarding charge carrier density estimation. Initial results suggest that there is a direct correlation between Raman shift and impurity concentration.

In this paper, we present a primary experimental and theoretical study of the Raman spectrum of host CZTS and modified CZTS for a range of dopant concentrations and a wider array of laser power, to probe the surface and bulk states.

Materials and methods

Synthesis of doped CZTS thin films

Thin antimony-doped CZTS films were electrochemically grown on a fluorinated tin oxide (FTO) substrate using a bath containing ions of interest (Cu^{2+}, Zn^{2+}, Sn^{2+}, and Sb^{3+}). Co-electrodeposition was done using a three-electrode cell connected to a Gamry Instruments Reference 600 potentiostat operated by virtual front panel software. For synthesis of zinc–copper–tin–antimony alloy, the as-deposited thin film, 50 ml of electrolyte containing copper sulfate pentahydrate, tin chloride, zinc sulfate and antimony trichloride were utilized. To control preferential electroplating, potassium sodium tartrate was utilized as a complexing or chelating agent to bring electrode potentials of different metal ions close in the electrolyte (or plating solution) ion complexes. The electrodeposition was carried out at ~ -1.6 V. Time of electrodeposition was limited to ~ 160–180 s, in order to obtain a 1–1.5-μm thick as-deposited film. The precursor films were annealed (duration ~ 2 h) in an evaporated sulfur environment to obtain a copper–antimony–zinc–tin–sulfide thin film. Sulfurization was carried out in a tube furnace (temperature ~ 550 °C) in an argon environment. Similar experiments were performed to get Ag- and Fe-doped CZTS films. Control experiments were also conducted without any antimony

doping. Sb-doped CZTS nanocrystals were prepared using solvothermal process as discussed in earlier reports [6].

Laser induced breakdown spectroscopy (LIBS) of modified CZTS thin films

A LIBS system was utilized for elemental analysis of Cu–Zn–Sn–Sb–S thin films. The LIBS system was equipped with LASER PHOTONICS YOL 1024 LASER system. For spectra collection, Avantes-AVS-USB 2.0 spectrophotometer system was utilized. AvaSoft 8.0 was utilized for recording of LIBS spectra. Line identifications were done using PLASUS Specline software.

Raman characterization of modified CZTS thin films

Raman spectra were obtained using an R 3000 QE Raman spectrometer (made by Raman Systems). A 785 nm laser was used for excitation. The laser power was varied from 90 to 290 mW for different sets of experiments. The wavelength stability of Raman spectrometer was good as the drift was less than ~ 1 cm^{-1} for over a 12-h period. The signal to noise ratio was ~ 1000:1 at full signal. The optical resolution of system was ~ 0.14 nm. All the experiments were performed in the backscattering geometry, focusing on the wavenumber range from 50 to 400 cm^{-1}. Peak parameters were obtained by least square Lorentzian fitting using Peakfit® software.

Atomic force microscopy of CZTS and modified CZTS thin films

Atomic force microscopy was performed using a JPK Instruments NanoWizard AFM (maximum scan volume $\sim 100 \times 100 \times 15$ μm^3, tip scanning system) on an inverted microscope (make : Zeiss AxioObserver). Cantilever was BudgetSensor Multi75E-G sample ($f = 75$ kHz, $k = 3$ N/m, Pt/Cr coating). Some images were also acquired using a Asylum Infinity 3D AFM. For imaging of doped and undoped sample, quantitative imaging (based on a fast force curve) with a combination of conductive AFM was used. For the conductivity image, drawing the maximum recorded current from each force curve was used. The bias voltage for measurement was ~ 10 V.

Results and discussion

Scanning electron microscopy (SEM) characterization results

The surface SEM imaging of Sb-doped CZTS thin film was performed using an FEI NanoNova scanning electron
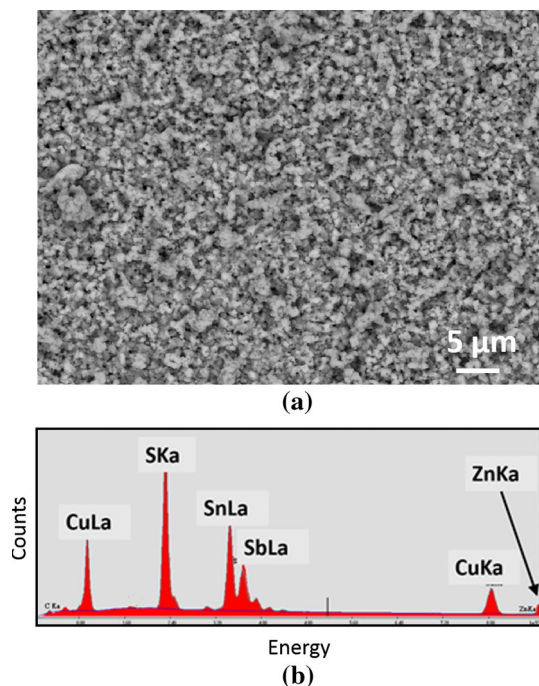
Fig. 1 a Scanning electron micrograph and **b** EDS spectrum of Sb-doped CZTS thin film

Fig. 2 a Laser induced breakdown spectroscopy experimental setup; **b** LIBS spectra for Sb-doped CZTS films

microscope. This film appears uniform without pit holes or cracks. Primary elemental characterization was done using energy dispersive spectroscopy (EDS). Figure 1a shows a scanning electron micrograph of 1 % Sb-doped CZTS thin film. An EDS spectrum is also shown in the inset of Fig. 1b.

Analysis of LIBS spectra

Figure 2a shows a LIBS system utilized for spectra acquisitions. Figure 2b shows LIBS spectra of antimony-doped CZTS films. It can be seen that entire spectral range (200–700 nm) is investigated. However, for antimony detection, 200–320 nm regions were explored in more depth. All characteristic Sb atomic transition lines were observed, which perfectly match with known wavelengths as discussed in the literature. Most of the characteristic peaks show a systematic change in peak intensity when Sb concentration in film increases. Antimony atomic emission lines are reported at $\sim$252.8, 259.8, 277, 287, and 303 nm [22]. In our experiment, most of these lines were observed, and the strongest was lined at 303.1 nm. A systematic change in line intensity was observed when concentration of Sb increased.

Analysis of shift in peak frequency

Raman spectra of doped CZTS thin film suggest a shift in several intense vibrational modes. It has been reported that
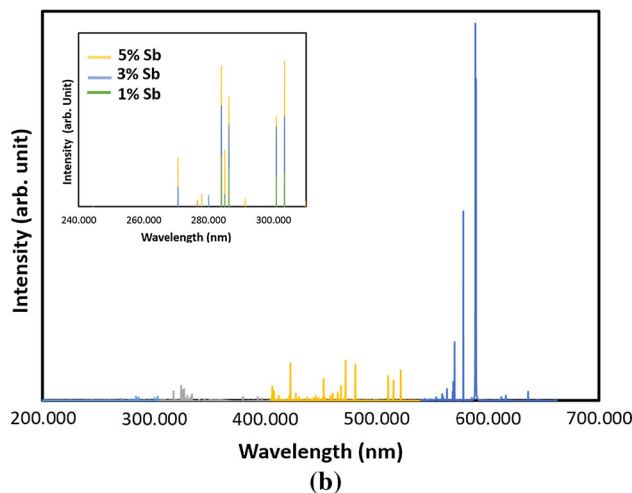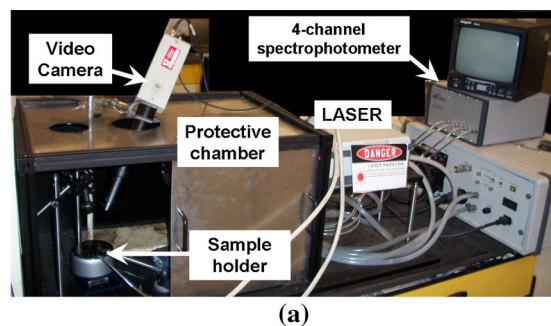
electronic and vibrational properties of semiconductors can be significantly changed by incorporation of impurities. Less massive foreign impurity atoms show local vibrational modes [23, 24]. These LVMS generally show sharp peaks in Raman spectra.

For a monoatomic linear chain, if one lattice atom of mass M is replaced by a smaller atom of mass m [24]:

$$\omega^2 = \omega_{\max}^2 \frac{M^2}{2Mm - m^2}, \tag{1}$$

Here,

$$\omega_{\max} = \left(\frac{4k}{M}\right)^{1/2}. \tag{2}$$

Here, ω is frequency of vibration, and k is spring force constant. This equation suggests that there is a square-root relationship between frequency and vibrating mass. In the case of a diatomic system, this relationship is still true; however, the reduced mass of the system will be taken into account. It should be noted that the frequency of 'A' Mode of vibration depends on the atomic weight ratio of their respective elements. For the kesterite group of compounds, A_2BCD_4 and W_2XYZ_4, it can be written, based on information from literature, that [25]:

$$\left(\frac{M_{\mathrm{D}}}{M_{\mathrm{Z}}}\right)^{1/2} = \frac{\omega_{\mathrm{A}(w_2 \mathrm{XYZ}_4)}}{\omega_{\mathrm{A}(\mathrm{A}_2 \mathrm{BCD}_4)}}. \tag{3}$$

This relationship suggests that Raman frequency will increase when weight of chalcogen decreases. This is the reason that one can observe higher frequency in the case of CZTS compared to CZTSe. Based on the literature, it can be written that [25]:

$$\frac{\left(\frac{M_{\mathrm{B}}+M_{\mathrm{C}}}{2}\right)^{1/2}}{\left(\frac{M_{\mathrm{X}}+M_{\mathrm{Y}}}{2}\right)^{1/2}} = \frac{\omega_{\mathrm{A}(w_2 \mathrm{XYZ}_4)}}{\omega_{\mathrm{A}(\mathrm{A}_2 \mathrm{BCD}_4)}}. \tag{4}$$

After considering the effects of anions and partial doping, Eq. 4 can be modified to

$$\frac{2M_{\mathrm{A}} + M_{\mathrm{B}} + (1-x)M_{\mathrm{C}}^1 + xM_{\mathrm{C}}^2 + 4M_{\mathrm{D}}}{2M_w + M_{\mathrm{X}} + M_{\mathrm{Y}} + 4M_{\mathrm{Z}}} = \frac{\omega_{\mathrm{undoped}}^2}{\omega_{\mathrm{doped}}^2}. \tag{5}$$

where $M_{\mathrm{A}}, M_{\mathrm{B}}, M_{\mathrm{C}}, \dots$etc., are atomic masses of constituent elements. x is a doping fraction. Now for partial substitution of zinc with antimony, it can be written as

$$\frac{439.17 + x\,(56.38)}{439.17} = \left(\frac{\omega_{\mathrm{undoped}}}{\omega_{\mathrm{doped}}}\right)^2. \tag{6}$$

Here, $\omega_{\mathrm{undoped}}$ and ω_{doped} are frequencies of A mode of vibration for undoped and doped CZTS samples. A detail investigation has been carried out to investigate Raman vibration modes of pure and doped CZTS samples. For undoped CZTS sample, no major peaks at 275, 352, 318, 267, 356, 215, 314, or 307 cm^{-1}, where secondary zinc sulfide, copper tin sulfide, and tin sulfide are found, were observed [11]. Thus, these phases are not dominant. In addition, no strong peaks at ~ 268 and 475 cm^{-1} were observed, which suggests that copper sulfide is not present at high concentration levels [11]. However, all strong CZTS peaks at ~ 335, 369, 289, and 253 cm^{-1} were observed, which suggest that high purity CZTS was obtained. The strong peaks at ~ 335 and 289 cm^{-1} can be assigned as A modes of vibration, whereas the peak at 255 cm^{-1} can be assigned as an E (TO, LO) mode of vibration [12]. There is a possibility of B modes of vibration, but these peaks did not appear due to the strong intensity of other peaks [12].

Figure 3a, b shows Raman 'A' and 'E' modes of vibration for different percentages of Sb doping. As expected, peak frequency of 'A' mode reduces when antimony doping is done. The simulated peak frequency also shifts toward lower wavenumber when doping increases. Using Eq. (6), a relationship between vibrational frequency for doped sample and undoped sample can be established, and an associated graph can be plotted. Figure 4 shows a comparison between experimental wavenumber shift and shift predicted
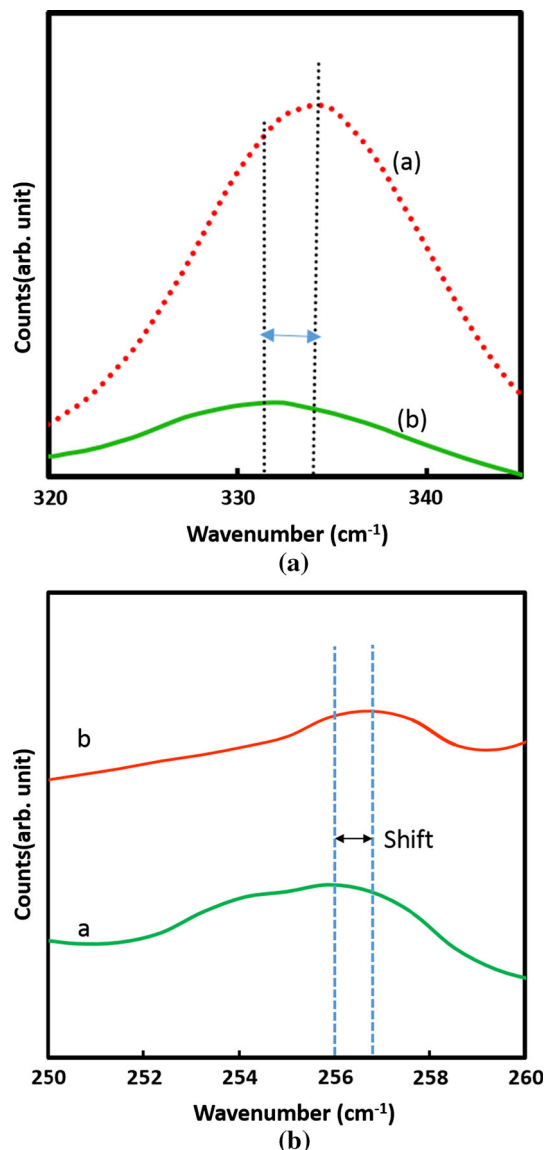

Fig. 3 a Shift in Raman 'A' mode was observed for different Sb concentrations *a* 1 %; *b* 3 %. **b** Shift in Raman E (TO, LO) mode was observed for different Sb concentrations *a* 5 %; *b* 1 %

by Eq. 6. Although there is a similar trend for frequency shift, a difference can be observed between simulated and experimental vibrational frequency. A possible reason for such a shift is formation of other phases, phonon confinement, and asymmetry due quantum interference. A shift of ~ 4 cm^{-1} suggests that the acceptor impurity can alter the position and line shape of phonons due to the strong correlation with charge carriers.

Ag- and Fe-doped CZTS films were also studied. Figure 5a shows Raman spectra of Fe-doped CZTS thin film with different amounts of Fe doping. It can be seen that the trend matches well with earlier reported Raman spectra [26]. Ag doping also causes a shift in Raman 'A' mode
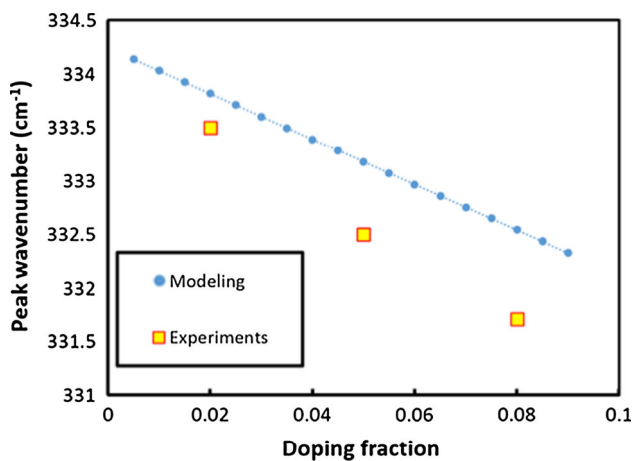
Fig. 4 Doping fraction-peak wavenumber relationship for Sb-doped CZTS films

peak frequency (See Fig. 5b). However, such a shift was not as significant as that observed for Sb doping. It is important to mention that Fe and Ag doping were not very helpful for better photo-response; however, Sb doping helps improving film quality and photoelectrochemical response. Hence, more focus was given to study Sb-doped CZTS thin film.

Investigation of local vibration modes and mode shift

A first principle-based study suggests that Raman scattering peaks at ~ 200–300 cm^{-1} are mainly due to vibrations associated with S and Zn/Sn [27]. Hence, peaks were identified in Raman spectra, which mainly represent Zn–S bonding states. Under this assumption, an investigation has been conducted to evaluate vibration modes associated with zinc-sulfur bonding or other substituted atom-sulfur bonds. It is known that antimony can occupy zinc sites for randomly substituted solid solution of zinc chalcogenides [9]. Hence for antimony-doped CZTS, it is very likely that antimony occupies zinc positions in the lattice. However, bonding of antimony with the neighboring sulfur (S) is expected to be different from that of original Zn–S bond.

In addition, there will be a change in the reduced mass due to such substitution. By calculation and estimation, the frequencies of the Sb-related local vibrational modes can be determined by taking into account the changes in reduced mass and force constant due to the substitution of Sb in the Zn lattice site. LVM frequency examination is an important tool for studying defects and low mass impurities in semiconductors. Here, it is important to mention that impurity modes can arise either due to differences in masses and force constants of dopants and host matrix or due to electron–phonon interactions [28]. Harmonic force constants can be calculated considering the effect of
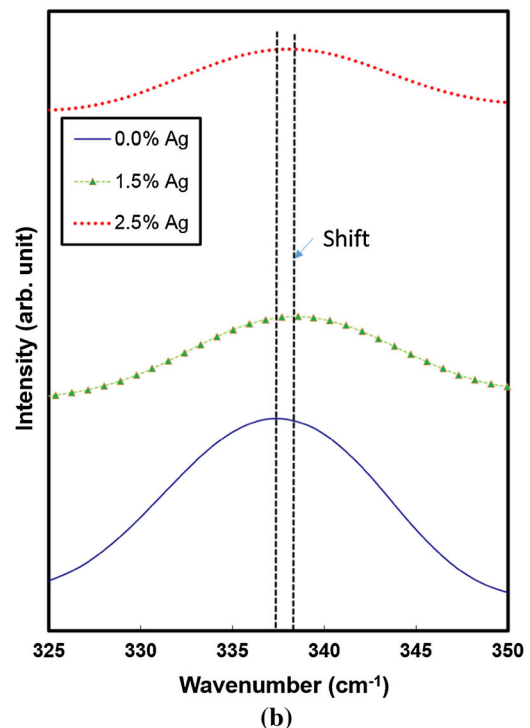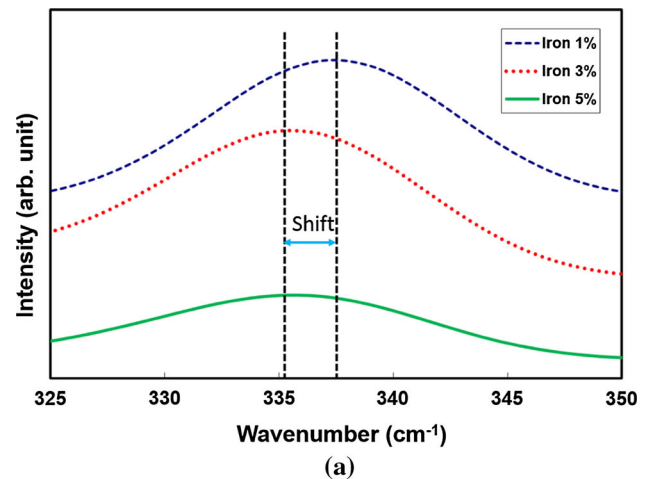

Fig. 5 **a** Raman spectra of Fe-doped CZTS films. **b** Raman spectra of Ag-doped CZTS films

interaction mass using the virtual-crystal approximation or quantum mechanical methods utilizing scale factor, s [24, 29–31]. The scaling factor s is a measure of the valence force parameter change in the vicinity of a defect [32]. The scaling factor approximation is a useful tool to describe interatomic forces due to central impurity atoms; it considers an equal relative change of all forces at the impurity atom with respect to pure crystal. The force constant varies with a change in interatomic distances [33]. For Zn–S bonds, the localized interatomic force constant change can be represented as [34]

$$f_{\text{localized (Zn–S)}} = \frac{f_{\text{localized (Sb–S)}}}{(1+s)}. \tag{7}$$

The reduced mass for an optical phonon (considering only Zn–S vibration) can be written as

$$\frac{1}{\mu} = \frac{1}{m_1} + \frac{1}{m_2}. \tag{8}$$

The impurity mode frequency can be given as

$$\left(\frac{\omega_{\text{Sb–S}}}{\omega_{\text{Zn–S}}}\right) = \sqrt{\left(\frac{\mu_{\text{Zn–S}}}{\mu_{\text{Sb–S}}}\right)} \times \sqrt{\left(\frac{f_{\text{Sb–S}}}{f_{\text{Zn–S}}}\right)}. \tag{9}$$

After using appropriate values, it can be stated that

$$\omega_{(\text{Sb–S})} = \omega_{(\text{Zn–S})} \times (0.953) \times (1+s)^{1/2}. \tag{10}$$

Using a scaling factor of -0.85, (which is very close to scaling factor for Zn–O:Sb system, $s = -0.70$) the following can be obtained:

Frequency $= \omega_{(\text{Zn–S})} \times (0.953) \times (0.15)^{1/2}$,

or $\omega_{(\text{Sb–S})} = 91 \text{ cm}^{-1}$.

Hence, the frequency for local vibration modes is $\sim 91 \text{ cm}^{-1}$, the experimental results also suggest (See Fig. 6) the presence of LVMs around 91 cm^{-1}. A negative scaling factor suggests the lattice softening due to antimony doping. Shift and change in line shape were also observed (See Fig. 3b) for E (TO, LO) mode centered at $\sim 255 \text{ cm}^{-1}$ when the Sb concentration changed. A change in carrier concentration can also affect the elastic constant of the materials. It is believed that the occupancy of large-sized highly electropositive Sb^{3+} ions in a strongly electronegative environment created by the negatively charged neighboring sulfur ions in the kesterite/stannite structure
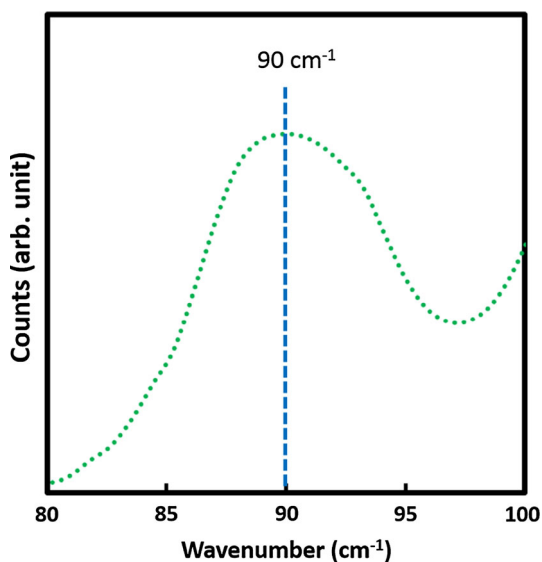

Fig. 6 Local Raman vibration mode at $\sim 90 \text{ cm}^{-1}$

causes the softening of the local lattice. Thus, the shift of Raman modes toward the lower energy side in CZTS:Sb is justified relative to undoped CZTS.

Observation of asymmetric line shape and the possibility of quantum interference between two competing optical pathways

The line shape of CZTS:Sb 'A' mode at room temperature (RT) is compared with that of CZTS in Fig. 7a, b. An 'A' mode of CZTS (Fig. 7a) fits reasonably well to a Lorentzian function, with a linear base line. On the other hand, in CZTS:Sb, the Lorentzian fit was not satisfactory due to the asymmetric line shape (See Fig. 7b). A Fano interaction can be a possibility for the origin of asymmetric line shape; however, no direct evidence of the Fano effect has been reported for this type of system till date. In the case of the assumption of the Fano effect, the Raman line shape changes due to the existence of a continuum of electronic excitations generated by inter-valence band transitions whose energy overlaps that of the zone-centered optical phonon. The Fano line shape is given as

$$F(q, \Gamma) = \mathbf{B} \frac{(q+\varepsilon)^2}{1+\varepsilon^2}; \text{ where } \varepsilon = \frac{\omega - \omega_o}{\Gamma} \tag{11}$$

ω_0 is the phonon frequency, q is the asymmetry parameter, Γ is the half-width parameter, and B is fitting parameter related with amplitude. For 5 % Sb-doped film, calculated fitting parameters (under assumption of Fano effect) were $|q| = 14.5$; line width $= 15.5$; $\Gamma_b/\Gamma_a = 1.32$.

It is important to note that for the Fano effect to occur, a continuum of energy states is needed. For undoped CZTS, some reports suggest the possibility of discrete states; however, information is limited [21]. Continuum of energy states is possible due to several reasons; one of them may be the presence of residual Sb, which is a semimetal, where free charge carriers can be found at Brillouin zone edges in pockets [35]. It was reported that interband intervalley transition is possible for Sb with a charge density of $\sim 10^{20} \text{ cm}^{-3}$. It can be seen that for Ag- and Fe-doped films, Raman peaks are more symmetric compared to Sb-doped CZTS film. All of these observations suggest that the Sb:CZTS system is different and needs more understanding and research, in order to evaluate its electronic and optical properties including a validation of quantum interference.

Effect of laser power on Phonon lineshape

In most of the cases, the role of laser power density and its effects on Raman line shape have been ascribed to changes in temperature. However, there are various factors that are responsible for changes in Raman spectra such as oxidation/degradation of material, strain, confinement effects,

Fig. 7 a Raman spectrum of 'A' mode of CZTS and associated Lorentz fitting; **b** Raman spectrum of A mode of 5 % Sb-doped CZTS film with Fano fitting
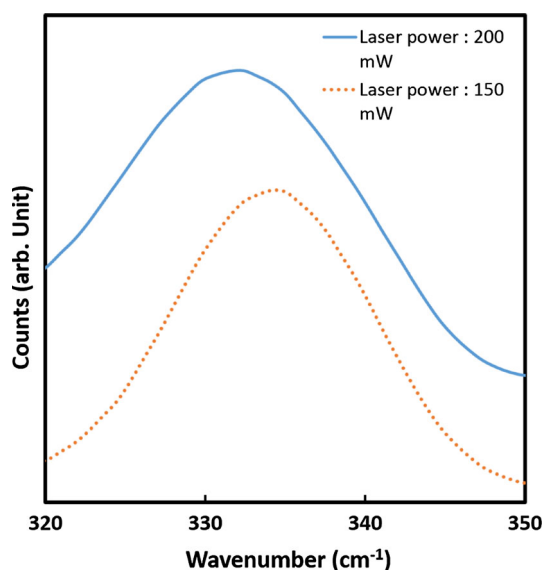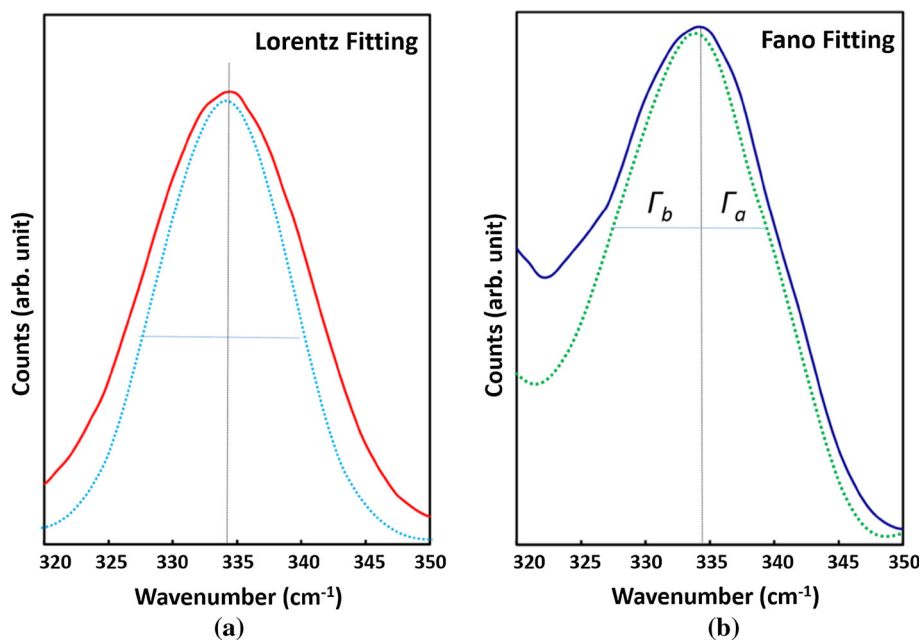

(a)

(b)

Fig. 8 Raman spectrum of A mode of CZTS: Sb recorded at different laser powers

Fig. 9 Raman spectra of 2 % Sb-doped CZTS nanocrystals

phase transitions, and/or Fano interactions. Figure 8 shows the Raman spectra of lightly ($\sim$1% Sb) doped CZTS thin film. Raman spectra show good reversibility during decreasing and increasing laser power. Increase in laser power causes broadening and red-shifting of spectra. A shift of $\sim$1.9 cm^{-1} was observed when laser power was increased from 150 to 200 mW. It was earlier observed that an average gradient for peak shift (extracted from a temperature–peak shift graph) $\frac{d\Delta\omega}{dT}$ was $\sim$0.0266 cm^{-1}/K [36]. This suggests that at least $\sim$75–80 °C change in temperature is needed for such a shift. However, measurement of

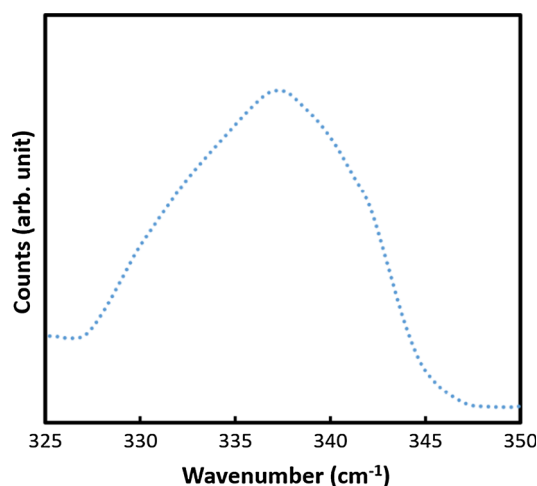temperature during spectra acquisition suggests that the thermal effect is not a major cause for it. Therefore, other causes for the observed shift can be strain, confinement effect, phase transition, or Fano interaction. Linewidth also changes when laser power changes. An increase in laser power from 150 to 200 mW causes a 3.1 cm^{-1} increment in linewidth. It has been reported that FWHM in Raman line shapes increases with increase in laser power density [37]. The asymmetry ratio for CZTS:Sb at relatively low laser power was $\sim$1.04, whereas a high asymmetry ratio $\sim$1.4 was observed at high laser power. At low laser power, observed asymmetry can be attributed due to quantum confinement, as there will be an insufficient number of photo-excited electrons. Hence, it is very likely

Fig. 10 Atomic force micrograph of doped and undoped CZTS samples: Topographic map of doped (**a**); and **b** undoped CZTS sample. **c** Electrostatic charge map for Sb-doped CZTS thin film. **d** Low magnification topographic map of doped; and **e** undoped CZTS sample. **f** Current map of doped; and **g** undoped CZTS sample. **h** Current map overlaid with topography for doped; and **i** undoped CZTS sample
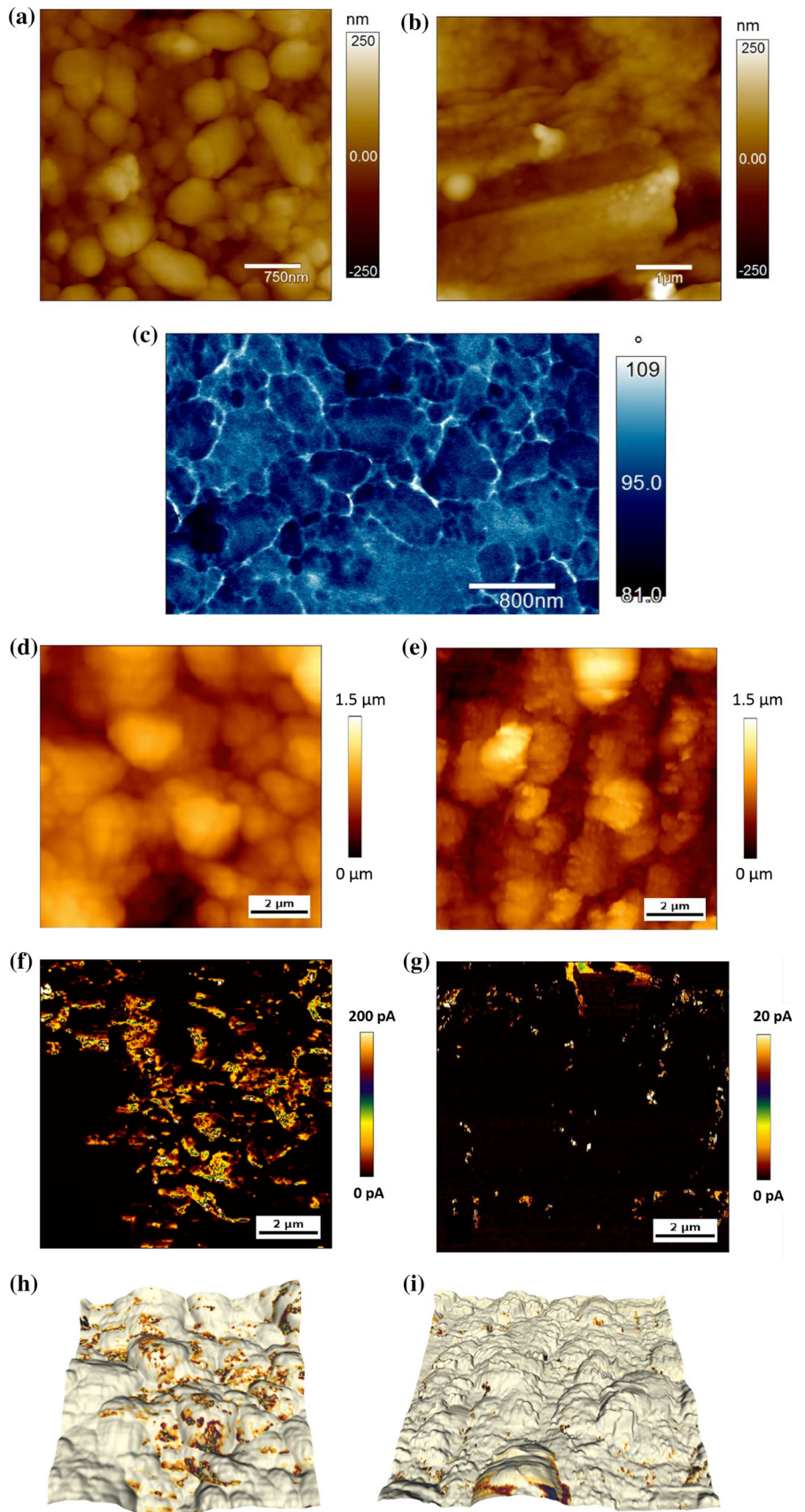
that the increase in asymmetry is due to the quantum interference between two competing optical pathways. The change in line shapes and asymmetry parameter is due to interactions between electronic Raman scattering of photo-excited electrons within electronic states and usual optical phonon Raman scattering. The electronic Raman contribution at higher laser power increases due to enhanced photo-excited electronic transitions. We also observed that at low laser power ~ 150 mW, linewidth of nanocrystalline sample is more comparable to bulk sample (See Fig. 9). Asymmetry is also high for nanocrystalline sample compared to polycrystalline thin film. Phonon confinement along specific directions of nanocrystals results in a breakdown of bulk Raman selection criteria. In this situation, other phonons in similar branches are activated and cause asymmetric broadening and shifting of the Raman peak. It can be seen that the Raman peak is asymmetric toward the lower frequency side. This asymmetry can arise due to the factors such as an inhomogeneous charge distribution within the laser spot [38]. However, such distribution causes more Raman peak broadening along the higher frequency side (near the charge neutrality point). On the contrary, in our case, asymmetry was observed toward the lower frequency side (in polycrystalline as well as nanocrystals); hence, the possibility of asymmetry due to inhomogeneous charge distribution is low. Another explanation of asymmetry along lower frequency is that the incident photon energy is close to the energy of an optical transition from a localized state. It was concluded that inhomogeneous broadening of the primary CZTS Raman line can be best described by a Gaussian line shape. Following this approach, there is possibility that our CZTS is a mixture of two phases (Kesterite and Stannite), and their ratio can be calculated based on their relative Raman cross section [39]. However, Ag- and Fe-doped CZTS film Raman line shapes eliminate this possibility.

Atomic force microscopy of Sb-doped and undoped CZTS film

Figure 10a–i shows topographical image, current image, and image containing 3D topography overlaid with current, respectively. It can be observed that with similar bias voltage, Sb-doped CZTS shows less current (compared to undoped sample), which shows lower conductivity. Electrostatic force microscopy was also performed on Sb-doped CZTS sample. The contrast in a electrostatic charge map can be clearly seen as a phase shift in resonance frequency of the tip. It can be seen that charge density is higher along grain boundaries compared to grains. It has been reported that grain size improvement and better device performance are possible when Sb doping (~ 0.2–1.0 %) is performed for copper indium gallium selenide (CIGS) thin film [40].

Higher Sb doping results in stronger preferred orientations along the (220)/(204) crystallographic direction [40]. Our atomic force microscopy examination suggests that there is a clear improvement in CZTS grain size when doped with Sb. It can be seen (See Fig. 10a–i) that undoped CZTS film contains some large grains, but they are surrounded by smaller grains, which appear sticky and agglomerated. However, in Sb-doped CZTS film, there are very few small grains associated with big grains. Topography suggests that big grains are greater than 1 μm in diameter. It was further observed that a larger grain size is achievable using Sb doping in relatively lower concentration, less time, and lower temperature. An electrically benign nature of grain boundaries was reported when Cu–Sb–S was used [41]. Advantages of Sb include lower cost compared to indium and the observation of a better absorbance coefficient of Cu-Sb-S compared to CZTS. Hence, it can be said that there is a possibility of better performance when CZTS is Sb doped. AFM characterization results indeed strengthen this observation.

Conclusions

Raman characterization of Sb-, Fe-, and Ag-doped CZTS was conducted. Raman shift was higher for Sb- and Fe-doped film compared to Ag-doped CZTS film. It was observed that Raman 'A' mode is asymmetric, and Lorentz fitting is not appropriate for Sb-doped CZTS thin films. Some observation suggests that Sb doping possibly creates a continuum of energy states and subsequent transition. Sb-doped CZTS nanocrystals also show similar characteristics, but asymmetry is much higher. The addition of Sb causes a lowering in peak wavenumber for Raman 'A' mode of vibration. Such an observation matches with theoretical prediction based on the change in effective mass. Increase in laser power causes broadening and red-shifting of spectra. A shift of ~ 1.9 cm^{-1} was observed when laser power was increased from 150 to 200 mW. Atomic force microscopy suggests that Sb-doped CZTS film grain boundaries are more conductive compared to CZTS thin-film grain boundaries. An improvement in CZTS grain boundary uniformity and size was observed when Sb doping is performed.

References

1. Todorov TK, Tang J, Bag S, Gunawan O, Gokmen T, Zhu Y, Mitzi DB (2013) Beyond 11 % efficiency: characteristics of

state-of-the-art Cu2ZnSn(S, Se)4 solar cells. Adv Energy Mater 3:34–38

2. Nagoya A, Asahi R, Wahl R, Kresse G (2010) Defect formation and phase stability of Cu_2ZnSnS_4 photovoltaic material. Phys Rev B 81:113202

3. Sarswat PK, Free ML (2012) An evaluation of depletion layer photoactivity in Cu_2ZnSnS_4 thin film. Thin Solid Films 520:4422–4426

4. Salomé PMP, Fernandes PA, da Cunha AF, Leitão JP, Malaquias J, Weber A, González JC, da Silva MIN (2010) Growth pressure dependence of $Cu_2ZnSnSe_4$ properties. Sol Energy Mater Sol Cells 94:2176–2180

5. Dimitrievska M, Fairbrother A, Pérez-Rodríguez A, Saucedo E, Izquierdo-Roca V (2014) Raman scattering crystalline assessment of polycrystalline Cu_2ZnSnS_4 thin films for sustainable photovoltaic technologies: phonon confinement model. Acta Mater 70:272–280

6. Sarswat PK, Free ML (2013) An investigation of rapidly synthesized Cu_2ZnSnS_4 nanocrystals. J Cryst Growth 372:87–94

7. Tablero C (2012) Electronic and photon absorber properties of Cr-doped Cu_2ZnSnS_4. J Phys Chem C 116:23224–23230

8. Moore J, Hages C, Lundstrom M, Agrawal R (2012) Influence of Ge doping on defect distributions of $Cu_2Zn(Sn_x Ge_{1-x}) (S_y Se_{1-y})$ fabricated by nanocrystal ink deposition with selenization Photovoltaic Specialists Conference (PVSC), 38th IEEE, 3–8 June 2012, pp 001475–001480

9. Sarswat PK, Free ML (2013) Enhanced photoelectrochemical response from copper antimony zinc sulfide thin films on transparent conducting electrode. Int J Photoenergy 2013:7. doi:10. 1155/2013/154694

10. Tsuyoshi M, Satoshi N, Takahiro W (2012) First-principles study on Cd doping in Cu_2ZnSnS_4 and $Cu_2ZnSnSe_4$ Japanese. J Appl Phys 51:10NC11

11. Fernandes PA, Salomé PMP, da Cunha AF (2011) Study of polycrystalline Cu_2ZnSnS_4 films by Raman scattering. J Alloy Compd 509:7600–7606

12. Dumcenco D, Huang Y-S (2013) The vibrational properties study of kesterite Cu_2ZnSnS_4 single crystals by using polarization dependent Raman spectroscopy. Opt Mater 35:419–425

13. Burke BG, Chan J, Williams KA, Wu Z, Puretzky AA, Geohegan DB (2010) Study of Fano interference in p-type doped silicon. J Raman Spectrosc 41:1759–1764

14. Kroner M, Govorov AO, Remi S, Biedermann B, Seidl S, Badolato A, Petroff PM, Zhang W, Barbour R, Gerardot BD, Warburton RJ, Karrai K (2008) The nonlinear Fano effect. Nature 451:311–314

15. Fano U (1961) Effects of configuration interaction on intensities and phase shifts. Phys Rev 124:1866–1878

16. Svidzinsky AA, Dorfman KE, Scully MO (2011) Enhancing photovoltaic power by Fano-induced coherence. Phys Rev A 84:053818

17. Zhang Y, Chen X, Ouyang Z, Lu H, Jia B, Shi Z, Gu M (2013) Improved multicrystalline Si solar cells by light trapping from Al nanoparticle enhanced antireflection coating. Opt Mater Express 3:489–495

18. Bellani V, Viña L, Hey R, Ploog K (1996) Modification of Fano resonances by resonant polaron coupling in bulk GaAs. Semicond Sci Technol 11:1411

19. Li W, Jiang K, Zhang J, Chen X, Hu Z, Chen S, Sun L, Chu J (2012) Temperature dependence of phonon modes, dielectric functions, and interband electronic transitions in Cu_2ZnSnS_4 semiconductor films. Phys Chem Chem Phys 14:9936–9941

20. Catlow CRA, Sokol AA, Walsh A (2013) Computational approaches to energy materials. Wiley, Chichester, pp 1–28

21. Bhatia A (2013) Laser annealing and defect study of chalcogenide photovoltaic materials. Department of Materials Science and Engineering, University of Utah

22. Hussain T, Gondal MA (2013) Laser induced breakdown spectroscopy (LIBS) as a rapid tool for material analysis. J Phys Conf Ser 439:012050

23. Ramsteiner M, Wagner J, Ennen H, Maier M (1988) Resonance Raman scattering of Si local vibrational modes in GaAs. Phys Rev B 38:10669–10676

24. McCluskey MD (2000) Local vibrational modes of impurities in semiconductors. J Appl Phys 87:3593–3617

25. Roy S, Guha P, Kundu SN, Hanzawa H, Chaudhuri S, Pal AK (2002) Characterization of Cu(In, Ga)Se2 films by Raman scattering. Mater Chem Phys 73:24–30

26. Fontané X, Izquierdo-Roca V, Saucedo E, Schorr S, Yukhymchuk VO, Valakh MYa, A Pérez-Rodríguez (2012) Vibrational properties of stannite and kesterite type compounds: Raman scattering analysis of $Cu_2(Fe,Zn)SnS_4$. J Alloy Compd 539:190–194

27. Khare A, Himmetoglu B, Johnson M, Norris DJ, Cococcioni M, Aydil ES (2012) Calculation of the lattice dynamics and Raman spectra of copper zinc tin chalcogenides and comparison to experiments. J Appl Phys 111. doi:10.1063/1.4704191

28. Romcevic N, Popovic ZV, Khokhlov DR (1995) Raman scattering spectra of indium-doped PbTe. J Phys Condens Matter 7:5105

29. Broser I, Kaczmarczyk G, Thurian P, Heitz R, Hoffmann A (1996) Local vibrational modes of the CuO_4-cluster in ZnO. J Cryst Growth 159:889–892

30. Haller EE (2005) Isotopically controlled semiconductors. Solid State Commun 133:693–707

31. Sundius T (2002) Scaling of ab initio force fields by MOLVIB. Vib Spectrosc 29:89–95

32. Kalescky R, Zou W, Kraka E, Cremer D (2012) Local vibrational modes of the water dimer—comparison of theory and experiment. Chem Phys Lett 554:243–247

33. Postnikov AV, Pagès O, Hugel J (2005) Lattice dynamics of the mixed semiconductors (Be,Zn)Se from first-principles calculations. Phys Rev B 71:115206

34. Samanta K, Arora AK, Katiyar RS (2012) Local vibrational modes and Fano interaction in p-type ZnO: Sb system. J Phys D Appl Phys 45:185304

35. Lemonnier JC, Thomas J, Robin S (1973) Optical properties and electronic structure of antimony in the energy range 2.5–14.5 eV. J Phys C 6:3205

36. Sarswat PK, Free ML, Tiwari A (2011) Temperature-dependent study of the Raman A mode of Cu_2ZnSnS_4 thin films. Phys Status Solidi (b) 248:2170–2174

37. Kumar R, Shukla A, Mavi H, Vankar V (2008) Size-dependent Fano interaction in the laser-etched silicon nanostructures. Nanoscale Res Lett 3:105–108

38. Casiraghi C, Pisana S, Novoselov KS, Geim AK, Ferrari AC (2007) Raman fingerprint of charged impurities in graphene. Appl Phys Lett 91:233108

39. Scragg JJS, Choubrac L, Lafond A, Ericson T, Platzer-Björkman C (2014) A low-temperature order-disorder transition in Cu_2ZnSnS_4 thin films. Appl Phys Lett 104:041911

40. Yuan M, Mitzi DB, Liu W, Kellock AJ, Chey SJ, Deline VR (2009) Optimization of CIGS based PV device through antimony doping. Chem Mater 22:285–287

41. http://meetings.aps.org/link/BAPS.2014.MAR.F24.1. Accessed 07 Nov 2014